Sample-Induced RF Perturbations in High-Field, High-Resolution NMR Spectroscopy

Stuart Crozier, Ian M. Brereton, Fernando O. Zelaya, Wolfgang U. Roffmann, and David M. Doddrell

Centre for Magnetic Resonance, University of Queensland, St. Lucia, Queensland 4072, Australia

Conducting dielectric samples are often used in high-resolution experiments at high field. It is shown that significant amplitude and phase distortions of the RF magnetic field may result from perturbations caused by such samples. Theoretical analyses demonstrate the spatial variation of the RF field amplitude and phase across the sample, and comparisons of the effect are made for a variety of sample properties and operating field strengths. Although the effect is highly nonlinear, it tends to increase with increasing field strength, permittivity, conductivity, and sample size. There are cases, however, in which increasing the conductivity of the sample improves the homogeneity of the amplitude of the RF field across the sample at the expense of distorted RF phase. It is important that the perturbation effects be calculated for the experimental conditions used, as they have the potential to reduce the signal-to-noise ratio of NMR experiments and may increase the generation of spurious coherences. The effect of RF-coil geometry on the coherences is also modeled, with the use of homogeneous resonators such as the birdcage design being preferred. Recommendations are made concerning methods of reducing sample-induced perturbations. Experimental high-field imaging and high-resolution studies demonstrate the effect. © 1997 Academic Press

INTRODUCTION

It is well known in medical MR imaging that the sample (the patient) distorts the RF B_1 field generated by the probe and absorbs RF energy. These effects arise from both the conductivity and permittivity of tissue (*1–8*) and are important for both safety and RF homogeneity considerations. The heterogeneity of tissue properties and the complex distribution of interfaces make accurate analytical modeling of these effects very difficult (*8*).

High-resolution liquid samples, however, are usually homogeneous and can be quite simply modeled. The purpose of this work is to investigate sample-induced RF perturbation effects when performing high-field, high-resolution, multipulse experiments. Many high-resolution experiments rely on consistent RF phase and flip angles across the sample. Inaccuracies in flip angles may be accounted for, in part, by appropriate phase cycles, which essentially attempt to cancel

unwanted signals arising from inaccurate flip angles or other effects. Often phase cycles are used to select particular coherence types. For a chemical compound exhibiting spin–spin coupling, spatial heterogeneity in the RF phase will lead to the generation of spatially dependent coherences during multipulse experiments which, at the least, may degrade the signal-to-noise ratio (SNR) of the experiment and, at the worst, can lead to the generation of spurious coherences. If both RF amplitude and phase distortions exist across the sample, then the efficacy of phase cycling may be reduced.

The origin of the distorted B_1 field can be either inherent inhomogeneities in the RF coil itself and/or sample-induced perturbations (neglecting transmitter and other spectrometer-based errors). Here we consider samples with a range of conductivities, permittivities, sizes, and irradiation at various frequencies as well as the use of either saddle-type RF coils or birdcage resonators. We have recently shown that birdcage resonators may be effectively designed and fabricated for high-resolution applications (*9*).

THEORETICAL BACKGROUND

Much of the preliminary theoretical work for this problem has been developed and applied to human imaging studies (*1–7*). Consider the geometry shown in Fig. 1. The field components inside a long cylinder exposed to a transverse RF polarizing field in polar coordinates (*1, 2*) are

$$B_r(r, \phi) = \frac{2B_1(r)I_1(Kr)}{I_0(Ka)Kr} \sin \phi \qquad [1]$$

$$B_\phi(r, \phi) = \frac{2B_1(r)}{I_0(Ka)} \left[I_0(Kr) - \frac{I_1(Kr)}{Kr} \right] \cos \phi, \quad [2]$$

where $B_r(r, \phi)$ and $B_\phi(r, \phi)$ are the orthogonal resultant field vectors (Fig. 1), $B_1(r)$ is the applied transverse field, $I_0(Kr)$ and $I_1(Kr)$ are modified Bessel functions of the first kind of zero and first order, respectively, a is the sample radius, and K is the wavenumber. As K is complex, the
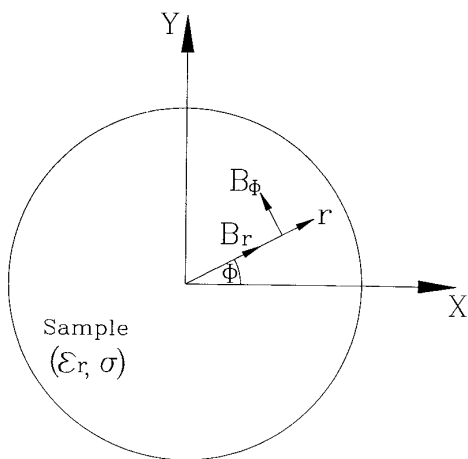
FIG. 1. The sample geometry and coordinate system.

modified Bessel functions are also complex and some care is required in their evaluation. Where the sample conductivity is small enough to be neglected, this situation simplifies considerably (7).

The complex wave number is represented as

$$K = \alpha + j\beta, \qquad [3]$$

where α is termed the attenuation constant (Np/m) and β is the phase constant (rad/m) (10). In terms of the sample parameters,

$$\alpha = \omega\sqrt{\mu\epsilon}\sqrt{\frac{1}{2}\left[\sqrt{1 + \left(\frac{\sigma}{\omega\epsilon}\right)^2} - 1\right]} \qquad [4]$$

$$\beta = \omega\sqrt{\mu\epsilon}\sqrt{\frac{1}{2}\left[\sqrt{1 + \left(\frac{\sigma}{\omega\epsilon}\right)^2} + 1\right]}, \qquad [5]$$

where ω is the angular frequency of operation, μ is the permeability, ϵ is the permittivity, and σ is the conductivity of the sample. Also,

$$\epsilon = \epsilon_r\epsilon_0, \qquad [6]$$

where ϵ_0 is the permittivity of free space and ϵ_r the relative permittivity or dielectric constant. By evaluating [1]–[6] for a particular sample, we obtain solutions for $B_\phi(r, \phi)$ and $B_r(r, \phi)$; it is more convenient to view these spatial dependencies in Cartesian coordinates, i.e.,

$$B_y(x, y) = B_r(r, \phi)\sin\phi + B_\phi(r, \phi)\cos\phi$$
$$B_x(x, y) = B_r(r, \phi)\cos\phi - B_\phi(r, \phi)\sin\phi. \qquad [7]$$

In all of the examples shown here, we assume, for simplicity, that the coil is linearly polarized (in the y direction); circular polarization may, however, be included in calculations of this nature (7). All field components described from here on are RF fields in the sample. Note that along the axes
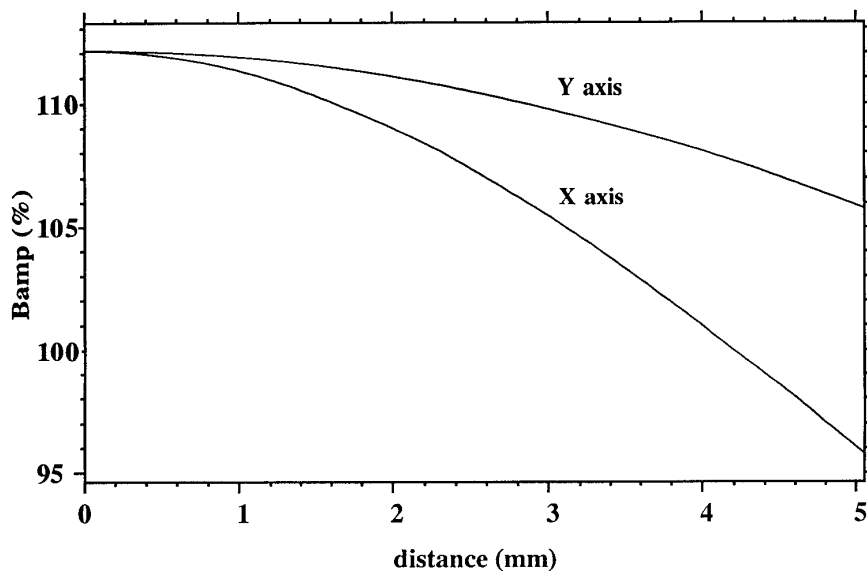

FIG. 2. The magnitude (B_{amp}) of the B_y RF magnetic field along X and Y axis radii in a sample of $\epsilon_r = 78$, $\sigma = 5$ S/m being irradiated at 750 MHz. The sample diameter is 10 mm. Distance is indicated from the origin.
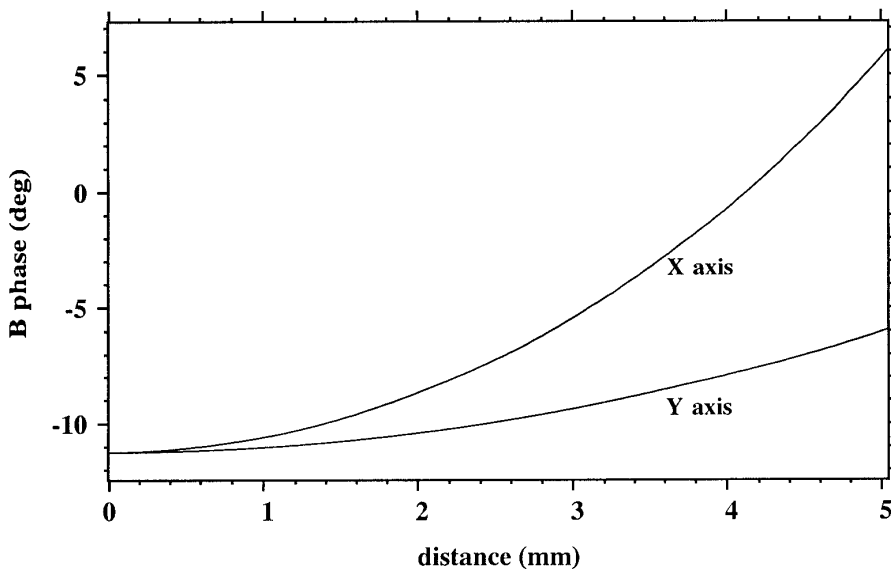
FIG. 3. Axial phase profiles of the B_y RF magnetic field in the sample described in the legend to Fig. 2. Distance is indicated from the origin.

of the sample, $B_y(y) = B_r(r, \phi)$ and $B_y(x) = B_\phi(r\phi)$ and that all field components are complex values.

SAMPLE-INDUCED PERTURBATIONS

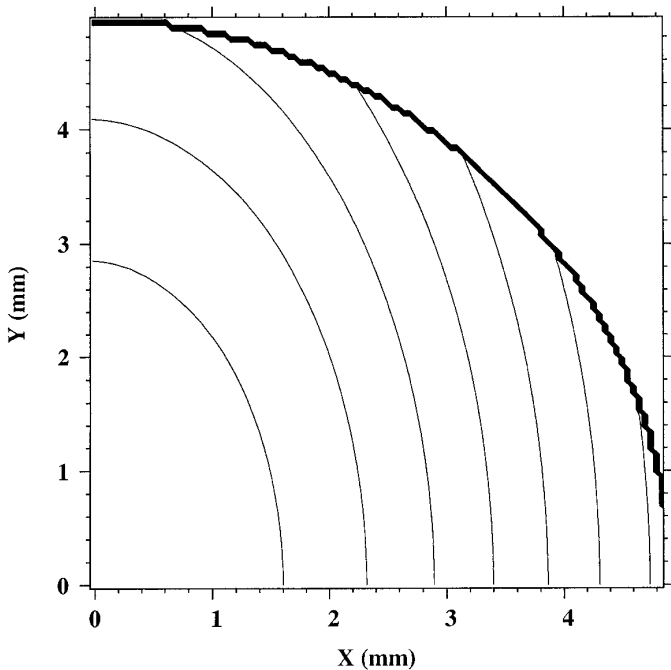We are now in a position to examine the effect of sample parameters on, e.g., $B_y(x, y)$. Much of the desire for op-

FIG. 4. Spatial variation of the magnitude of B_y RF magnetic field in one quadrant of the sample described in the legend to Fig. 2. Contours indicate 2% deviation from the central value (i.e., the value at the origin).

erating at high fields has come from the need for increased SNR and spectral resolution in ^{1}H NMR spectroscopy of proteins. These (and other samples) are often buffered in conducting solutions and may contain a large number of charges (*11*). A reasonably extensive range of conductivity for the purposes of this study of $1 < \sigma < 10$ S/m was chosen, while measurements of cytochrome C of concentrations 0.8– 4 m*M* in water indicate conductivities of 0.5–2.8 S/m (*12*). The dielectric constant of samples of this nature varies little from $\epsilon_r = 78$. Operating frequencies for ^{1}H NMR spectroscopy of 500 MHz, 750 MHz, and 1 GHz were chosen to cover existing and soon-to-be-available field strengths.

We begin with a sample of $\epsilon_r = 78$, $\sigma = 5$ S/m being irradiated at 750 MHz in a 10 mm tube. The amplitudes (B_{amp}) (Fig. 2) and phase (Fig. 3) of the resultant B_1 field along the Y and X axes show significant distortion, with the strongest effect being in a direction orthogonal to the polarizing field direction, in general agreement with previous results (*7*). The field at the origin is raised in this case by the effect of the damped standing wave. Figure 4 shows the spatial dependencies in one quadrant of the sample at 2% contour levels from the value at the origin for the field amplitude.

In order to compare a number of different effects on both the B_1 fields and the resultant signals, we now normalize the amplitude of the B_1 field to be 1.0 and the phase to be 0° at the origin. This is akin to the operator correctly setting a 90° pulse at 0° phase in the middle of the sample and is obviously a somewhat generous assumption as, when there is significant perturbation, the resultant signal (the volume integral across the sample) will be such that the 90° flip angle will be correctly set only for the average of the field.
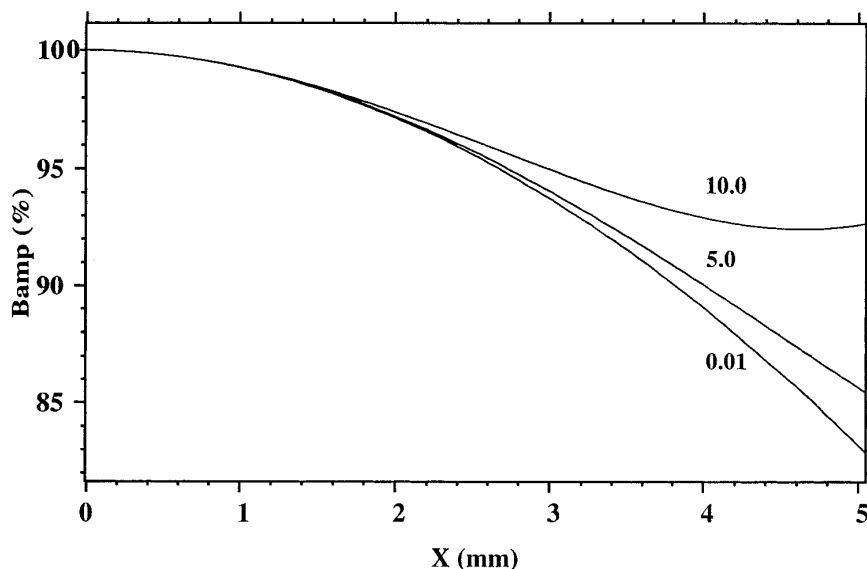
FIG. 5. The effect of sample conductivity on the normalized *X*-axis value of the magnitude of B_y.

For ease of comparison of both fields and signals, however, we make the prescribed normalization for all further results.

As the largest distortion tends to occur normal to the polarizing direction, we make some comparisons of $B_y(x)$ fields. Figure 5 shows the effect of sample conductivity in a 10 mm tube at 750 MHz, $\epsilon_r = 78$ on $B_y(x)$ amplitude, and Fig. 6 shows the effect on $B_y(x)$ phase. As the conductivity increases, so does the phase error across the sample. Note that at low conductivity ($< \sim 0.01$ S/m) there is very little phase variation as expected. The amplitude distortion, under

these conditions, actually decreases with increasing conductivity (Fig. 5), although this effect reverses itself at very high conductivities (and field strengths), where the amplitude at the edge of the sample increases dramatically. The effects of operating frequency on the field amplitude and phase are shown in Figs. 7 and 8, respectively, for a sample of $\epsilon_r = 78$, $\sigma = 5$ S/m in a 10 mm tube. The distortions increase strongly with operating frequency and become particularly severe for samples of diameter greater than 5 mm.

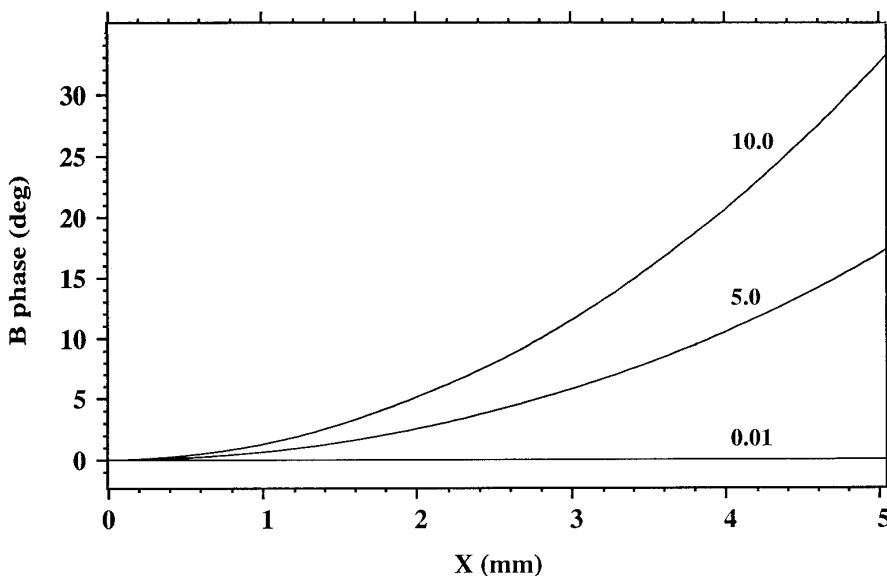We have demonstrated the strong perturbation effects that

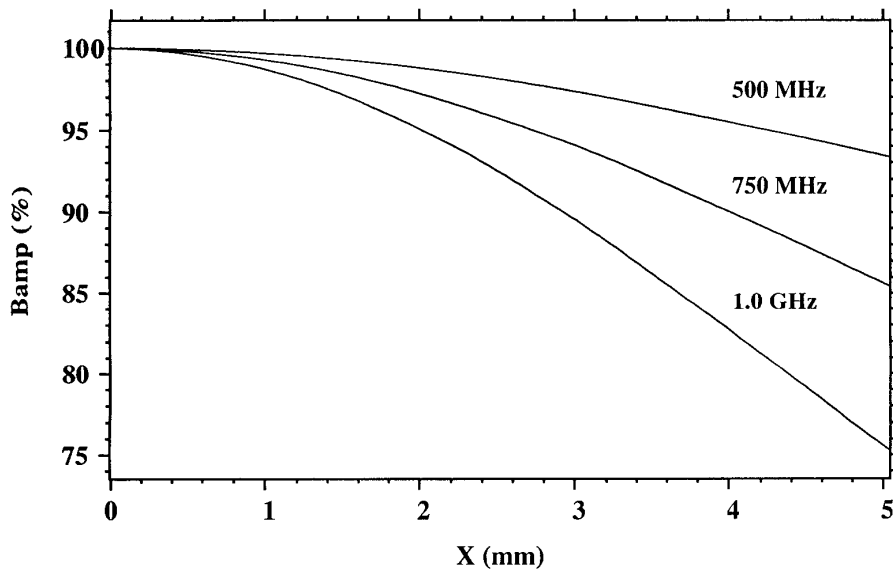**FIG. 6.** The effect of sample conductivity on the normalized *X*-axis value of the phase of B_y.

FIG. 7. The effect of operating frequency on the normalized *X*-axis value of the magnitude of B_y.

samples can have on B_1 fields. The effect on the acquired signal is usually even more pronounced than that on the field. The B_1 dependence of signal acquired from a pulse and collect experiment is simply

$$S(x, y) = S_0 B_y(x, y) \sin\left(\frac{\pi}{2} B_y(x, y) \right), \qquad [8]$$

where S_0 is a constant representing the signal at the center of the sample and remembering that B_1 is normalized to have

an amplitude of 1.0 and a phase of 0° at the origin. The resultant signal will, of course, be complex, and variations in B_1 amplitude and phase serve to reduce the SNR of the experiment and disrupt effective phase cycling.

CHOICE OF RF COIL

Apart from the sample perturbing the B_1 field, the RF coil generates its own inherent inhomogeneities. Fortunately, these generally affect only the amplitude of the RF fields
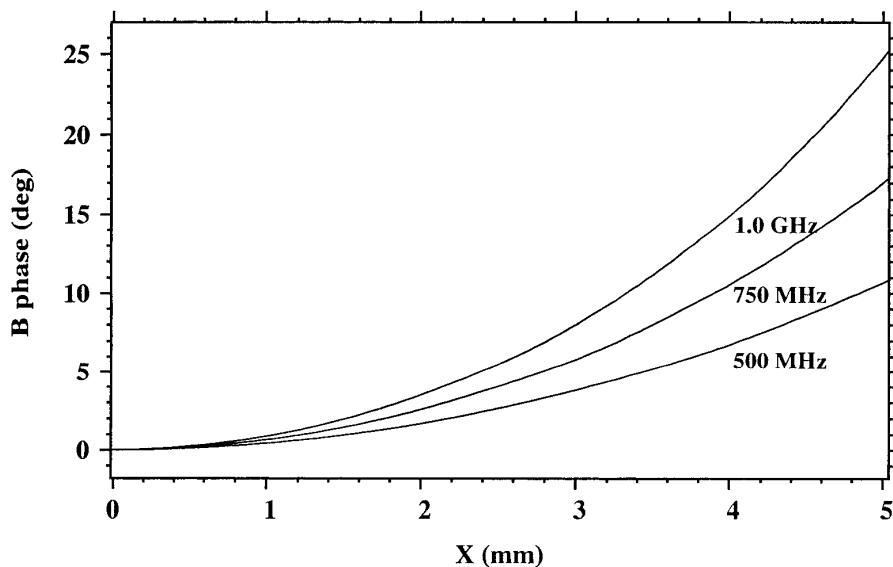

FIG. 8. The effect of operating frequency on the normalized *X*-axis value of the phase of B_y.
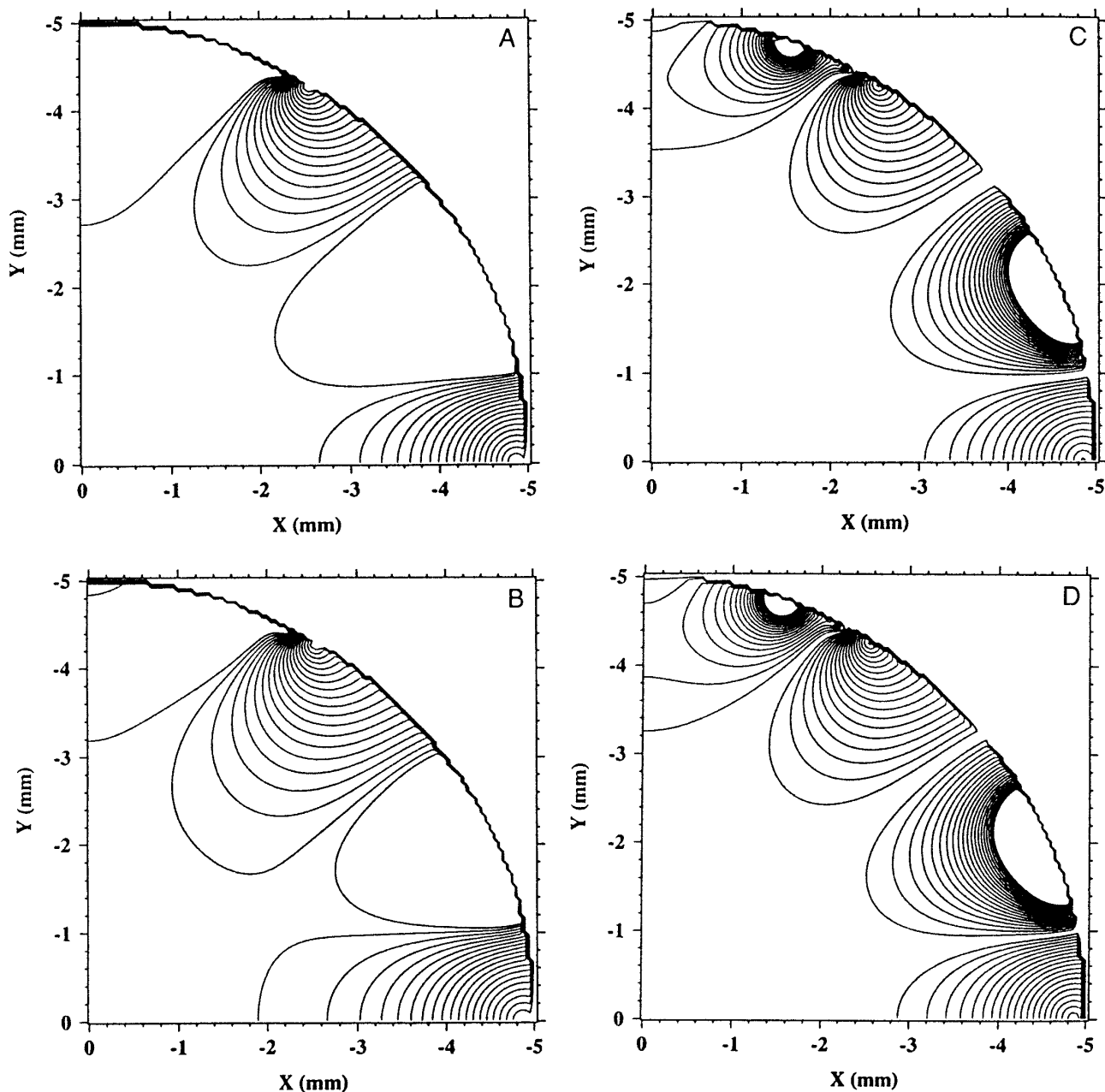
FIG. 9. The effect of using different RF coils. (A) and (C) are the 5% contours of the RF magnetic field generated by a saddle and birdcage coil, respectively. (B) and (D) are the resultant magnetic field when a sample of $\epsilon_r = 78$, $\sigma = 2$ S/m is inserted into the coils which are operating at 750 MHz. Note the superior performance of the birdcage system.

and not the phase. Figures 9A and 9C show contour plots of typical 10 mm saddle and birdcage coils, respectively. The B_1 fields in the coils were calculated including RF eddy currents and full-current densities on the streamline members (9). It is well known that the birdcage coil has homogeneity superior to saddle-type coils (13). We have recently shown that such coils can be effectively fabricated on small diameters (9, 14).

The inherent inhomogeneity of the RF coil may be combined with the sample perturbation calculations, and for a sample of $\sigma = 2$ S/m, $\epsilon_r = 78$ at 750 MHz, the resultant magnitude of the B_1 fields is shown in Figs. 9B and 9D for saddle and birdcage [8-rung interrung feeding (9)] coils, respectively, the result being clearly better for a birdcage coil. It is reasonable to expect that coherence generation and phase-cycling efficiency would concomitantly improve in
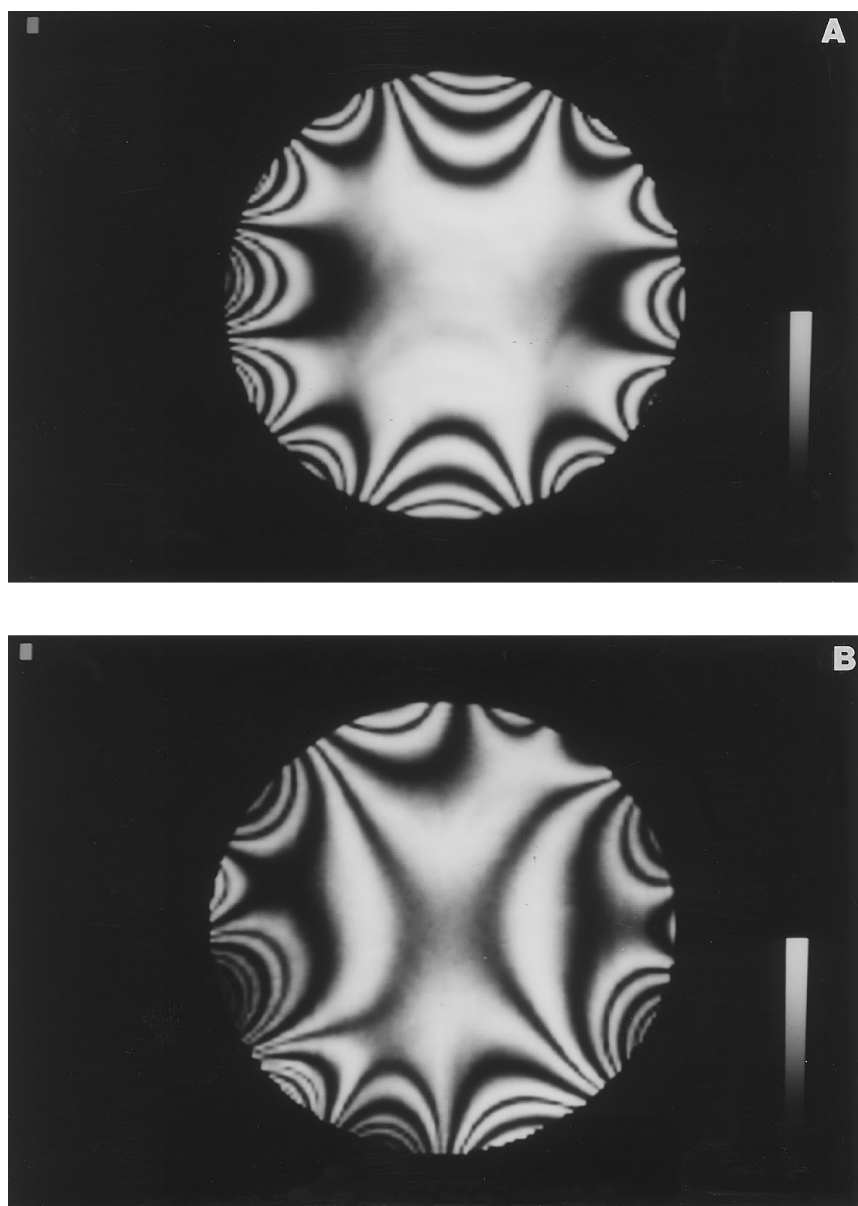
FIG. 10. The 300-MHz spin-echo B_1 maps of: (A) a low-conductivity, low-dielectric sample (silicon oil) and (B) a KCL solution of $\sigma = 2.5$ S/m, $\epsilon_r = 78$. In each case, 20 mm tubes were used. The dark bands indicate approximately 5% incremental deviations from linearity. The sequence used is described in detail in Ref. (*9, 15*).

this coil, but would still be adversely effected by sample-induced perturbations as noted above.

EXPERIMENTAL RESULTS

Much of the theory of sample perturbation has previously been rigorously tested for imaging applications at relatively low field strengths (*1–7*). In this work, we performed imaging experiments at 300 MHz and high-resolution experiments at 750 MHz. For the imaging experiments, the instru-ment used consisted of a 15 cm, 7 T Bruker magnet inter-faced to a Bruker AMX300 console. Custom-built shielded gradients sets and birdcage resonators were used. High-reso-lution experiments were performed on a Bruker DMX-750 console interfaced to a MAGNEX magnet. The Bruker probe used was an 8 mm triple-resonance, broadband inverse (TBI) type.

To illustrate the marked perturbation that samples may produce on RF fields, we compare B_1 maps of the type described in (*9, 15*) for 2.0 cm diameter samples of silicon

oil and 250 mM KCl. Figure 10 shows the difference between the maps of the magnitude of the RF fields; clearly the KCl sample ($\epsilon_r = 78$, $\sigma \approx 2.5$ S/m) significantly distorts the RF field (Fig. 10B). In both images, the inner most contour depicts a 5% deviation from homogeneity.

For conductive samples, in addition to amplitude variations in the RF field, phase variations are expected across the sample. These are more difficult to measure than amplitude variations. In order to illustrate these phase differences, we performed a series of conventional spin-echo experiments (TR/TE = 1000/20 ms, FOV = 3 cm, slice thickness 1 mm, 2 acquisitions) in 20 mm tubes of 4 samples all with $\epsilon_r = 78$, but whose conductivity varied ($\sigma = 10^{-3}$, 5.0, 10.0, 20.0 S/m). Phase images rather than magnitude-calculated 2DFTs were performed on the time-domain signals, and then the phase image from the reference sample (10^{-3} S/m) was subtracted from the other three in an attempt to remove those phase variations not associated with sample perturbation. From each of these three differential phase images, a histogram was made, this now represents the statistical spread of differential signal phase across the sample. Figure 11 shows the three histograms and demonstrates the nonlinearity of the effect.

Experimental verification of the spatial variation of B_1 amplitude and phase was attempted at 750 MHz using test samples consisting of an 8 mm o.d. NMR tube containing a solution of 20 mM acetamidophenol in 90% D_2O, into which was placed a 3 mm o.d. coaxial reference insert containing 100 mM glucose in the same solvent. For comparison with a highly conductive solvent, the same solutions were prepared with the addition of 2N KCl ($\sigma \approx 20$ S/m). The 360° pulse time was measured for each solution, by observing the solute resonances for each tube, placing the carrier frequency on-resonance for the respective sig-
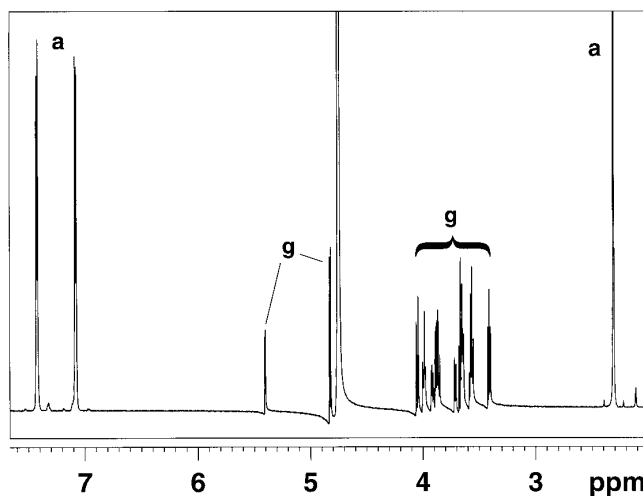

FIG. 12. A 750-MHz ^1H spectrum of test sample containing 2M KCl as described in the text. Peaks labeled a arise from acetamidophenol contained in the outer tube, and those labeled g, from glucose in the inner tube. The spectrum is the result of a single acquisition and was phase corrected by applying a zero-order correction to phase the upfield acetamidophenol CH_3 resonance; first-order adjustment was applied to phase the aromatic resonances. A phase difference of 13° was observed between the resonances originating from the different tubes. No phase difference was observed for the solutions not containing KCl.

nals. The difference in 360° pulse times observed between the inner and outer tubes was 1 μs (53.5 vs 52.5 μs) for the low-conductivity test sample, and 6 μs (284 vs 278 μs) for the highly conductive sample. A single-scan pulse-and-acquire spectrum of the first sample showed no phase difference between the resonances observed in each tube. However, as illustrated in Fig. 12, a distinct zero-order phase difference (13°) was observed between the tubes in the case of the 2N KCl solutions. The theoretical prediction for the phase difference was 15.5°.

CONCLUSION

We have demonstrated that samples used for high-resolution, high-field spectroscopy of high permittivity and conductivity can have a deleterious effect on the generated RF field across them and consequently can disrupt the generation of observed coherences. This problem is exacerbated as the field strength and sample diameter increase.

In order to reduce these effects, a simple but not often practical solution is to reduce the permittivity and conductivity of the sample. If this is not possible, it is preferable to restrict the diameter of the sample under investigation and to use homogeneous coils, with the birdcage-type volume resonator being preferred to saddle coils.
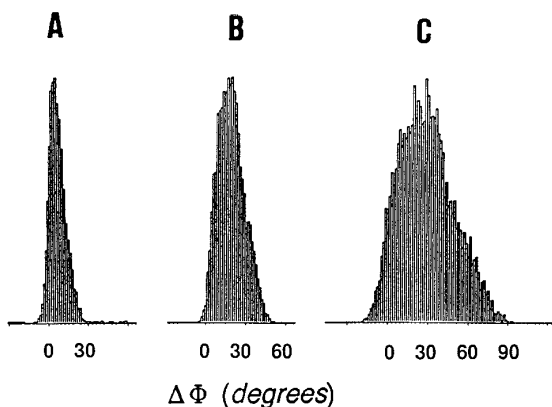
ACKNOWLEDGMENTS

FIG. 11. Histograms of the signal phase distributions in samples of different conductivity at 300 MHz with $\epsilon_r = 78$. The samples were imaged in 20 mm tubes and had conductivities of $\sigma = 5$, 10, and 20 S/m. The phase images were referenced to the same experiment performed in a nonconducting solution of $\epsilon_r = 78$.

REFERENCES

1. P. A. Bottomley and E. R. Andrew, *Phys. Med. Biol.* **23,** 630 (1978).

2. P. Mansfield and P. G. Morris, ''Advances in Magnetic Resonance,'' Suppl. 2, pp. 181–187, Academic Press, New York, 1982.

3. G. H. Glover, C. E. Hayes, N. J. Pelc, W. A. Edelstein, O. M. Mueller, H. R. Hart, C. J. Hardy, M. O'Donnell, and W. D. Barber, *J. Magn. Reson.* **64,** 255 (1985).

4. P. A. Bottomley, R. W. Redington, W. A. Edelstein, and J. F. Schenck, *Magn. Reson. Med.* **2,** 336 (1985).

5. T. K. F. Foo, C. E. Hayes, and Y.-W. Kang, *Magn. Reson. Med.* **23,** 287 (1992).

6. P. M. Joseph and M. Saadi-Elmandjra, *J. Magn. Reson.* **75,** 199 (1987).

7. P. Tofts, *J. Magn. Reson. B* **104,** 143 (1994).

8. L. S. Petropoulos, E. M. Haacke, R. W. Brown, and E. Boerner, *Magn. Reson. Med.* **30,** 366 (1993).

9. S. Crozier, K. Luescher, L. K. Forbes, and D. M. Doddrell, *J. Magn. Reson. B* **109,** 1 (1995).

10. C. A. Balanis, ''Advanced Engineering Electromagnetics,'' Wiley, New York, 1989.

11. G. C. K. Roberts, ''NMR of Macromolecules, A Practical Approach,'' IRL Press, Oxford, 1993.

12. G. Jones and B. C. Bradshaw, *J. Am. Chem. Soc.* **55,** 1780 (1933).

13. C. E. Hayes, W. A. Edelstein, J. F. Schenck, O. M. Mueller, and M. Eash, *J. Magn. Reson.* **63,** 622 (1985).

14. W. Roffmann, S. Crozier, K. Luescher, and D. M. Doddrell, *J. Magn. Reson.* **111,** 174 (1996).

15. F. O. Zelaya, W. U. Roffmann, S. Crozier, S. Teed, D. Gross, and D. M. Doddrell, *J. Magn. Imag.,* in press (1997).